JM PAPERS

The hidden structure of hydrodynamic transport in random fracture networks

Marco Dentz[1],† and Jeffrey D. Hyman[2]

[1]Spanish National Research Council (IDAEA-CSIC), 08034 Barcelona, Spain

[2]Computational Earth Science (EES-16), Earth and Environmental Sciences Division, Los Alamos National Laboratory, Los Alamos, NM 87545, USA

We study the large-scale dynamics and prediction of hydrodynamic transport in random fracture networks. The flow and transport behaviour is characterized by first passage times and displacement statistics, which show heavy tails and anomalous dispersion with a strong dependence on the injection condition. The origin of these behaviours is investigated in terms of Lagrangian velocities sampled equidistantly along particle trajectories, unlike classical sampling strategies at a constant rate. The velocity series are analysed by their copula density, the joint distribution of the velocity unit scores, which reveals a simple, albeit hidden, correlation structure that can be described by a Gaussian copula. Based on this insight, we derive a Langevin equation for the evolution of equidistant particle speeds. In this framework, particle motion is quantified by a stochastic time-domain random walk, the joint density of particle position, and speed satisfies a Klein–Kramers equation. The upscaled theory quantifies particle motion in terms of the characteristic fracture length scale and the distribution of Eulerian flow velocities. That is, it is predictive in the sense that it does not require the *a priori* knowledge of transport attributes. The upscaled model captures non-Fickian transport features, and their dependence on the injection conditions in terms of the velocity point statistics and average fracture length. It shows that the first passage times and displacement moments are dominated by extremes occurring at the first step. The presented approach integrates the interaction of flow and structure into a predictive model for large-scale transport in random fracture networks.

Key words: dispersion

† Email address for correspondence: marco.dentz@csic.es

1. Introduction

The dispersion of solutes and particles transported within laminar flow through random fracture networks is due to the complex network structure, which induces a strongly heterogeneous flow field. Dispersion in fracture networks is similar in nature to hydrodynamic dispersion in porous media (de Josselin de Jong 1958; Saffman 1959). From a Lagrangian view point, dispersion can be seen as the result of the correlated random motion of idealized solute particles moving with the flow. The spatial organization of the flow field reflects the topology and geometry of the fracture network, where the mean fracture length determines a characteristic scale of spatial variability. A result of this feature is that particle residence times in low-velocity regions can be orders of magnitude larger than residence times in high-velocity ones, which is one possible explanation for the observations of broad spectra of travel times in field studies (Becker & Shapiro 2000; Meigs & Beauheim 2001; Kang *et al.* 2015) and numerical simulations (Berkowitz & Scher 1997; Hyman *et al.* 2015). A quantitative understanding of these processes leading to the prediction of solute dispersion and travel time distributions through fracture networks is a key issue for diverse applications throughout engineering and science, including groundwater management (Viswanathan *et al.* 2022), geological sequestration of carbon dioxide (Hyman *et al.* 2019*c*), restoration of contaminated aquifers (Neuman 2005), the underground storage of radioactive waste (Hadgu *et al.* 2017), the understanding of speleogenesis (Dreybrodt, Gabrovšek & Romanov 2005; Maqueda, Renard & Filipponi 2023), and the prediction of flow and transport in karst aquifers (Goeppert, Goldscheider & Berkowitz 2020).

Experimental and numerical data show that first passage time distributions in fractured media almost invariably display heavy tails with power-law scalings as $t^{-1-\beta}$ with $0 < \beta < 2$ (Becker & Shapiro 2000; Haggerty *et al.* 2001; Painter, Cvetkovic & Selroos 2002). Such phenomena cannot be modelled analytically using classical Fickian transport models because the fundamental assumptions of a stable homogenization volume and fast relaxation times are violated in many natural systems. Thus different approaches have been proposed to interpret and analyse the observations. Continuous time random walk (CTRW) (Berkowitz & Scher 1997; Kang *et al.* 2011) and time-domain random walk (TDRW) (Delay & Bodin 2001; Benke & Painter 2003; Bodin, Porel & Delay 2003; Painter & Cvetkovic 2005) approaches model advective particle transport through spatial transitions of variable duration; see also the review paper by Noetinger *et al.* (2016). The transition times are calculated kinematically from characteristic travel distances and the flow velocity (Berkowitz & Scher 1997; Benke & Painter 2003; Kang *et al.* 2011), which reflects the fact that the flow field is organized on fixed length scales. Other CTRW approaches obtain the transition time distributions by calibration of parametric models to observed solute breakthrough curves (Berkowitz *et al.* 2006; Geiger, Cortis & Birkholzer 2010). Matrix-diffusion (Małoszewski & Zuber 1985) and multirate mass transfer approaches (Haggerty & Gorelick 1995; Carrera *et al.* 1998) model transport under diffusive mass transfer between flowing regions, the fracture domain, and stagnant regions, the rock matrix. Strong tailing of solute breakthrough curves is traced back to broad distributions of retention times. The impact of spatially variable flow velocity and matrix retention has been modelled by coupled TDRW and trapping models (Hyman *et al.* 2019*d*; Hyman & Dentz 2021).

The ubiquity of power-law tails in solute breakthrough curves suggests that there may be a universal behaviour (Berkowitz & Scher 1997; Becker & Shapiro 2000; Haggerty *et al.* 2001; Hyman *et al.* 2019*a*). However, the dependence of the power exponents on

the network properties (Hyman *et al.* 2019*b*) and on the injection conditions (Hyman *et al.* 2015; Kang *et al.* 2017; Hyman & Dentz 2021) seems to suggest otherwise. For a uniform solute injection over the inlet, the tailing of observed breakthrough curves is more pronounced than for flux-weighted injections, that is, if the solute mass injected is proportional to the local volumetric flow rate. This juxtaposition indicates that it is possible to formulate an approach that quantifies the evolution of large-scale transport in random fracture networks from arbitrary initial conditions. Moreover, we hypothesize that the origin of these behaviours can be found in the structure that is imprinted into Lagrangian velocity series.

In this study, we address these fundamental questions through detailed numerical simulations of flow and transport in a three-dimensional random fracture network. In order to identify the stochastic nature of particle motion through the network, we perform a Lagrangian analysis of particle velocities sampled equidistantly along streamlines (Dentz *et al.* 2016). Unlike sampling at constant frequency in time, this strategy reflects the fact that particle velocities and trajectories fluctuate on the spatial scales imprinted in the fracture network rather than a constant fluctuation time scale. In fact, velocity series sampled at constant frequency in porous media display intermittent behaviour characterized by long periods of low-velocity and short periods of high-velocity fluctuations (De Anna *et al.* 2013; Morales *et al.* 2017). Spatial sampling removes this intermittency and renders velocity series that can be represented as Markov processes. Here, we analyse the correlation structure of the spatial velocity series in terms of the copula density (Nelsen 2013; Haslauer, Bárdossy & Sudicky 2017; Massoudieh, Dentz & Alikhani 2017) of subsequent particle velocities. Based on this analysis, we identify the structure of Lagrangian velocity series, and formulate a stochastic transport model, as well as the evolution equation for the distribution of particle position and speed in form of a Klein–Kramers equation. This approach addresses the dependence of transport on both the flow distribution and network structure, and the initial conditions. It captures the large-scale physics of hydrodynamic transport in the network, and explains the propagation of transport from an arbitrary initial condition.

The article is organized as follows. Section 2 describes the random fracture networks under consideration, the fundamental flow and transport equations, and the numerical simulations to solve them. Also, it defines the target observations. Section 3 presents the stochastic analysis of particle trajectories and speed series, and their formulation in a large-scale transport model. Section 4 uses the derived model to shed light on the behaviour of the travel time distributions and displacement moments obtained from the detailed numerical simulations.

2. Flow and transport in fracture networks

In the following, we describe the network generation, the governing equations of flow and advective particle motion. Furthermore, we define the observables of interest and the set-up of the numerical simulations.

2.1. *Random fracture networks*

We consider a generic network composed of uniformly sized square fractures with edge length 2 m. The network is generic in the sense that it is not based on a particular field site; rather, it is designed to mimic a densely fractured disordered medium (Bonnet *et al.* 2001; Hyman & Jiménez-Martínez 2017; Mourzenko, Thovert & Adler 2011;
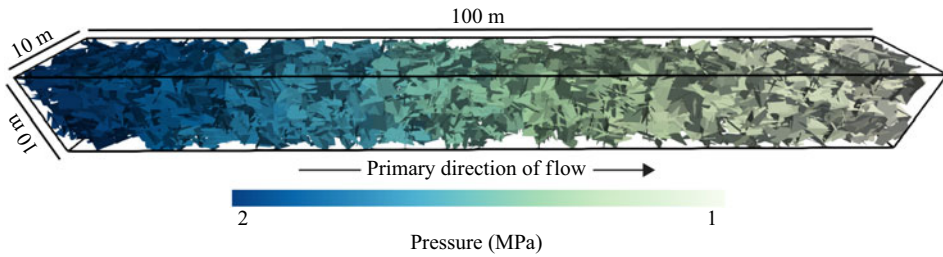
Figure 1. Three-dimensional discrete fracture network composed of 5660 fractures. Fractures are coloured by pressure.

Viswanathan *et al.* 2022). The network is generated as follows. Initially, 12 000 fractures are placed randomly into a cuboid domain of dimensions 100 m × 10 m × 10 m. Fracture centres are distributed uniformly throughout the domain, and orientations are uniformly random, that is, normal vectors are distributed uniformly on the surface of the unit sphere. The hydraulic aperture of each fracture is constant within each fracture and is the same for all fractures, 10^{-5} m. Isolated fractures and clusters of fractures are removed from the domain as they do not participate in the flow. The final network, illustrated in figure 1, contains 5660 fractures. The model medium is sufficiently large to quantify the impact of network heterogeneity in longitudinal large-scale transport. Due to computational limitations, the longitudinal extension of the domain is much larger than the transverse. Additional details of network generation are provided in the supplementary material available at https://doi.org/10.1017/jfm.2023.973.

2.2. *Fracture flow*

2.2.1. *Flow within a single fracture*

We begin by considering flow through a single fracture. The laminar flow of an incompressible isothermal Newtonian fluid within a fracture is described by the Stokes equations

$$\mu \, \nabla^2 \boldsymbol{u} - \nabla P = 0, \quad \nabla \cdot \boldsymbol{u} = 0. \tag{2.1a,b}$$

Here, $\boldsymbol{u}$ is the velocity vector, μ is the dynamic viscosity, and ∇P is the fluid pressure gradient.

The fracture aperture is assumed to be constant and equal to b, which is small compared to the horizontal fracture extension. Moreover, we assume that the matrix surrounding the fractures is impervious, and there is no interaction between flow within the fractures and the solid matrix. Under these conditions, fracture flow is equivalent to flow through a Hele-Shaw cell, and the flow velocities can be approximated locally as quadratic functions of the vertical coordinates (Batchelor 2000). Thus integration of the flow field across the aperture yields for the volumetric flow rate per unit length of fracture $\boldsymbol{Q}$ the Darcy-type equation

$$\boldsymbol{Q} = -T \, \nabla P, \tag{2.2}$$

where $T = b^3/12\mu$ is the fracture transmissivity, which is known as the cubic law. Thus we are representing the fractures as two-dimensional planes with resistance to flow proportional to the cube of the hydraulic aperture. Because flow is incompressible, volume is conserved such that $\nabla \cdot \boldsymbol{Q} = 0$. Volume conservation together with (2.2) gives the

977 A38-4

Reynolds equation

$$\nabla \cdot (T \, \nabla P) = 0 \tag{2.3}$$

for the pressure distribution in the fracture. The assumptions concerning surface roughness, Reynolds number and fluid properties required to arrive at (2.3) are detailed in Zimmerman & Bodvarsson (1996). The flux in each fracture is given by $q = Q/b$, which satisfies

$$q = -\frac{k}{\mu} \, \nabla P, \tag{2.4}$$

where the fracture permeability is defined by $k = b^2/12$.

2.2.2. *Flow within a fracture network*

Once fractures are placed into a network with other fractures, local boundary conditions modify the structure of the internal flow field within a single fracture, even in the case of a uniform hydraulic aperture. Specifically, the geometry of fractures, their boundaries and location of intersections within, along with network connectivity, leads to the formation of spatially variable velocity fields within a fracture plane even when flow is resolved using (2.3) on two-dimensional planar fractures. Neumann no-flow boundary conditions are imposed on the perimeter of all fractures and normal to the fracture plane; that is, there is no flow into the matrix. Within the network, pressure is a continuous and differentiable field that requires that pressure continuity along fracture intersections is imposed (Berre, Doster & Keilegavlen 2019). Likewise, the flow volumetric rate needs to be divergence-free along intersections for an incompressible fluid. Note that the flux need not be continuous across the line of intersection. This discontinuity occurs if the values of apertures on the two intersecting fractures differ. The governing equations return values for the volumetric flow rate Q, flux q and pressure P throughout the network. To resolve transport, we need the spatially variable Eulerian velocity field $u = q/\phi$, where ϕ is the fracture porosity. Here, porosity is set to 1, that is, the fractures are fully open.

The probability density function (p.d.f.) of the Eulerian flow speed $v_e(x) = |u(x)|$ is a key quantity, as detailed below. It is defined through volumetric sampling as

$$p_e(v) = \frac{1}{V} \int_{\Omega} \mathrm{d}x \, \delta[v - v_e(x)], \tag{2.5}$$

where V is the volume of the flow domain Ω.

2.3. *Particle motion*

In this study, particle motion within the fracture network is due to advection only. We use a Lagrangian point of view and describe the transport of a solute particle starting at the point a by the kinematic equation

$$\frac{\mathrm{d}x(t; a)}{\mathrm{d}t} = u[x(t; a)]. \tag{2.6}$$

Molecular diffusion and mass exchange between fracture and matrix are not taken into account. It does impact the mean transport behaviour in the network. Furthermore, longitudinal dispersion is dominated by the network heterogeneity.

The distribution of a solute entering the fracture network is described typically using one of two conceptualizations, namely resident-based and flux-weighted injection

(Kreft & Zuber 1978). Physically, resident-based injection corresponds to a source that introduces a solute uniformly throughout an input area. For this reason, it is also referred to as uniform injection. In contrast, flux-weighted injection corresponds to a solute released in proportion to the inflowing volumetric flow rate at a location of insertion. These two injection modes are known to result in different transport behaviours through both fractured and heterogeneous porous media (Vanderborght, Mallants & Feyen 1998; Demmy, Berglund & Graham 1999; Frampton & Cvetkovic 2009, 2011; Gotovac, Cvetkovic & Andricevic 2009, 2010; Janković & Fiori 2010; Hyman *et al.* 2015; Kang *et al.* 2017, 2020; Comolli, Hakoun & Dentz 2019; Puyguiraud, Gouze & Dentz 2019). In this work, we study the transport behaviours emerging from both injection modes.

For the uniform injection, the initial particle positions are distributed uniformly across the fractures in the injection plane such that the initial particle density is $\rho(\boldsymbol{a}) = 1$. For the flux-weighted injection, the initial particle density is

$$\rho(\boldsymbol{a}) = \frac{Q(\boldsymbol{a})}{\langle Q \rangle}, \tag{2.7}$$

where $Q(\boldsymbol{a}) = |\boldsymbol{Q}(\boldsymbol{a})|$ is the magnitude of $\boldsymbol{Q}$, and $\langle Q \rangle$ is its average across the injection plane.

2.4. *Observables*

Macroscale transport through the fracture network is characterized by the distribution of particle arrival times, or breakthrough curves at different control planes within the network, as well as the longitudinal displacement mean and variance. The first passage or arrival time $\tau(x'; \boldsymbol{a})$ of a particle at a control plane located a linear distance x' in the primary direction of flow is defined by

$$\tau(x'; \boldsymbol{a}) = \inf\{t \mid x(t; \boldsymbol{a}) \geq x'\}. \tag{2.8}$$

Its distribution is given by

$$f(\tau, x') = \langle \rho(\boldsymbol{a}) \, \delta[\tau - \tau(x'; \boldsymbol{a})] \rangle, \tag{2.9}$$

where the angular brackets denote the average over all particles. We refer to (2.9) as the first passage time distribution or breakthrough curve. The displacement mean and variance are defined by

$$m_1(t) = \langle \rho(\boldsymbol{a}) \, x(t; \boldsymbol{a}) \rangle, \quad \sigma^2(t) = \langle \rho(\boldsymbol{a}) \, x(t; \boldsymbol{a})^2 \rangle - \mu(t)^2. \tag{2.10a,b}$$

2.5. *Numerical simulations*

Once the network is generated, a conforming Delaunay triangulation of the network is created using the methods presented in Hyman *et al.* (2014) and Krotz *et al.* (2022). An unstructured two-point flux finite-volume scheme is used to discretize the governing equations for flow (2.3). We apply Dirichlet boundary conditions for pressure to create a pressure difference $\Delta P = 1$ MPa to drive flow from the $x = 0$ m face of the domain to the $x = 100$ m face. The particular value of the pressure difference is arbitrary because the governing equations are linear in ∇P. Therefore, the structure of the steady flow field, which is our primary interest, does not change with different pressure differences. Only its magnitude changes, which can be rescaled arbitrarily for our purposes. The model set-up creates a single principal flow direction, from which the flow within fractures can deviate.
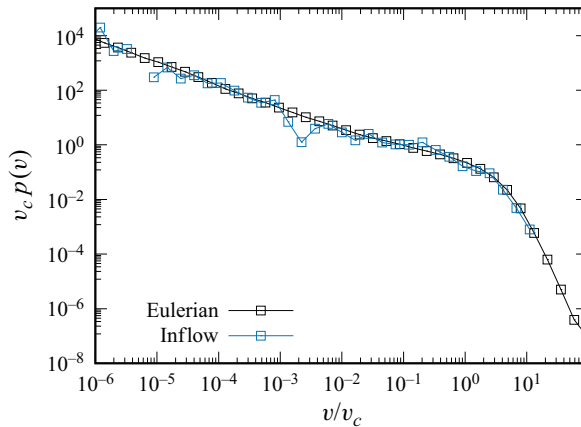
Figure 2. Eulerian velocity p.d.f.s for the entire network (black squares) and the inlet plane (blue squares). Speeds are rescaled by the Eulerian mean velocity v_c.

We use the massively parallel flow and reactive code PFLOTRAN (Lichtner *et al.* 2015) to integrate numerically the governing equations and obtain pressure and volumetric flow rates throughout the network, which are then used to reconstruct the Eulerian velocity field. Comprehensive details concerning the numerical simulations are provided in the supplementary material.

Figure 2 shows the Eulerian velocity distributions for the entire network and the inlet plane. The two distributions match well at the low-velocity end, but differ at high velocities. Thus the size of the injection plane is large enough to be representative of the global speed distribution at values smaller than the average speed. The undersampling of high speeds can be explained by the smaller probability to encounter speeds higher than the mean compared to speed smaller than the mean.

For the particle tracking simulations, we distinguish two sets of particles. In the first set, we follow 10^4 particles and record all Lagrangian information. That is, spatial location, velocity and time are retained at every time step. In the second set, we follow 10^6 particles and record their pathline length and travel time to reach uniformly spaced control planes placed at $\Delta x = 10$ m spacing through the domain. The use of different sets is a matter of computational limitations.

3. Stochastic particle dynamics

In this section, we analyse the stochastic dynamics of particle transitions and particle speeds. We first formulate the kinematic equations particle motion in terms of distance along streamlines, which honours the fact that particle speeds evolve on characteristic length rather than time scales. Then we analyse the correlation structure of subsequent particle velocities in terms of their copula density, with the aim of identifying an analytical model for speed transitions as an alternative to empirical transition matrices and to corroborate analytical modelling approaches. We find that speed series can be characterized by a stationary Gaussian copula. These insights are used to derive a stochastic TDRW model and the stochastic differential equations that govern the evolution of particle positions and speeds. Finally, we derive the corresponding CTRW model for displacements that are much larger than the characteristic length scale for the evolution of the particle speeds. The resulting CTRW model is conditioned on the distribution of initial velocities.
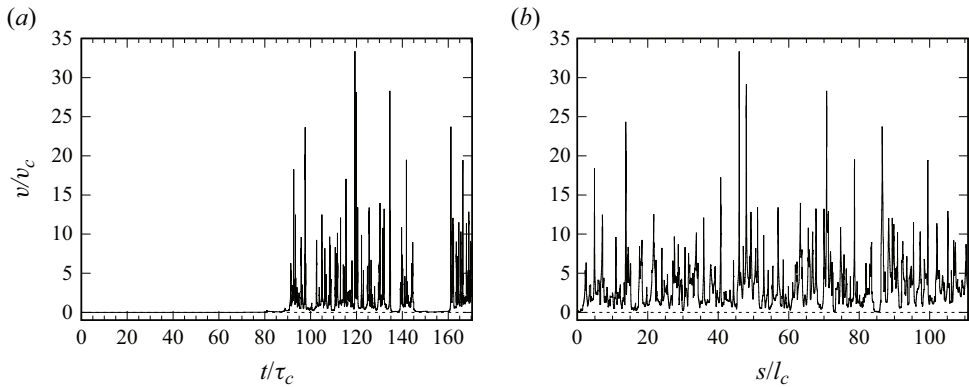
Figure 3. Evolution of particle speeds with (*a*) time and (*b*) distance along a trajectory.

3.1. *Kinematics*

Rather than evolving on a characteristic time scale, particle motion in disordered media evolves on the length scales imprinted in the medium structure (Dentz *et al.* 2016). For random fracture networks, the evolution scales are imposed by the network geometry and its hydraulic properties. This is illustrated in figure 3, which shows the series of particle speeds as a function of time and as a function of distance along a trajectory. Plotted against time, the speed series shows an intermittent pattern with long periods of low speeds and islands of high speeds. Flow speeds are organized on a characteristic length scale, which is of the order of the mean fracture length ℓ_c. Therefore, low velocities persist over much longer times than high velocities. In fact, plotted against distance, the speed series displays a regular random pattern that evolves on the scale of the mean fracture length ℓ_c. Thus in order to gain insight into the structure and organization of flow and transport, we analyse the particle dynamics as a function of distance along trajectories.

To this end, we note that the kinematic equation (2.6) can be formulated equivalently in terms of the distance $s(t; \boldsymbol{a})$ travelled by a particle along a streamline. The length $s(t; \boldsymbol{a})$ of the trajectory at a time t is given by

$$\frac{\mathrm{d}s(t; \boldsymbol{a})}{\mathrm{d}t} = v_e[\boldsymbol{x}(t; \boldsymbol{a})]. \tag{3.1}$$

We use $\mathrm{d}s = v(s; \boldsymbol{a})\,\mathrm{d}t$, where $v(s; \boldsymbol{a}) = v_e[\boldsymbol{x}(s; \boldsymbol{a})]$. For the kinematic equation (2.6), this gives

$$\frac{\mathrm{d}\boldsymbol{x}(s; \boldsymbol{a})}{\mathrm{d}s} = \frac{\boldsymbol{u}[\boldsymbol{x}(s; \boldsymbol{a})]}{v(s; \boldsymbol{a})}, \qquad \frac{\mathrm{d}t(s; \boldsymbol{a})}{\mathrm{d}s} = \frac{1}{v(s; \boldsymbol{a})}. \tag{3.2a,b}$$

We aim to quantify the stochastic dynamics of particle motion in the streamwise direction. We first focus on the motion along s, and specifically at the stochastic quantification of the series $\{v(s; \boldsymbol{a})\}$ of particle speeds.

3.2. *Stochastic dynamics of particle speeds: Markov model and transition probabilities*

In the following, we formulate the speed series $\{v(s; \boldsymbol{a})\}$ as a stationary Markov process and define its key statistics, the transition probability and the stationary speed distribution. We then analyse the structure of speed transitions using the copula densities that correspond to the empirical transition probabilities. Based on this analysis, we derive

977 A38-8

the resulting stochastic speed process that can be used to replace approaches based on empirical transition probabilities.

3.2.1. *Speed statistics and Markov model*

We represent the series $\{v(s; \boldsymbol{a})\}$ of particle speeds along a trajectory by the stochastic process $\{v(s)\}$, and replace the average over all particles by the ensemble average over all realizations of $v(s)$. Based on the random structure of the fracture networks under consideration, we pose $v(s)$ as a stationary Markov process continuous in s. This implies that the conditional probability $p(v, \Delta s|v')$ of two speeds separated by the lag distance Δs, the transition probability, obeys the Chapman–Kolmogorov equation (Risken 1996)

$$p(v, s|v') = \int_0^\infty \mathrm{d}v''\, p(v, \Delta s|v'')\, p(v'', s - \Delta s|v'), \qquad (3.3)$$

where $s \geq \Delta s$. The distribution $p(v, s)$ of particle speeds then evolves from any initial distribution $p_0(v)$ according to

$$p(v, s) = \int_0^\infty \mathrm{d}v'\, p(v, s|v')\, p_0(v'). \qquad (3.4)$$

The steady-state distribution $p_s(v)$ is an eigenfunction of $p(v, s|v')$. In the following, we refer to $p(v, s|v')$ also as the transition probability from v' to v. The Markov process is defined by two key quantities, the steady-state distribution $p_s(v)$ and the transition probability $p(v, s|v')$. Using Lagrangian ergodicity and the Reynolds theorem, it can be shown (Dentz *et al.* 2016) that $p_s(v, s)$ is given by the flux-weighted Eulerian speed distribution

$$p_s(v) = \frac{v\, p_e(v)}{v_c}, \qquad (3.5)$$

where $v_c = \langle v_e \rangle$ is the mean Eulerian speed. Equation (3.5) relates a Eulerian quantity and a Lagrangian quantity, that is, a flow attribute and a transport attribute. It is a key step for the prediction of transport based on transport-independent quantities such as medium structure and Eulerian flow distribution.

Equations (3.3) and (3.4) describe a spatial Markov model for particle velocities, in the sense that $v(s)$ is a velocity that evolves in distance along a trajectory. Spatial Markov models for the evolution of particle velocities and transition times have been used in the literature for the modelling of non-Fickian transport features in porous and fractured media (Sherman *et al.* 2021). The transition probabilities, which are at the head of these modelling approaches, are based typically on empirical transition matrices, which are obtained from particle tracking data. In the next subsubsection, we investigate the structure of spatial velocity transitions and their representation in terms of an analytical model.

3.2.2. *Structure of speed process: copulas*

The structure of the speed process $v(s)$, and thus the structure of hydrodynamic transport, is contained in the transition probability $p(v, s|v')$. In order to characterize $p(v, s|v')$, we focus on its copula density (Nelsen 2013), which encodes the information on the correlation properties of $\{v(s)\}$ without bias from the marginal distribution. The copula density is equal to the transition probability of the unit score transforms $u(s)$ of $v(s)$,
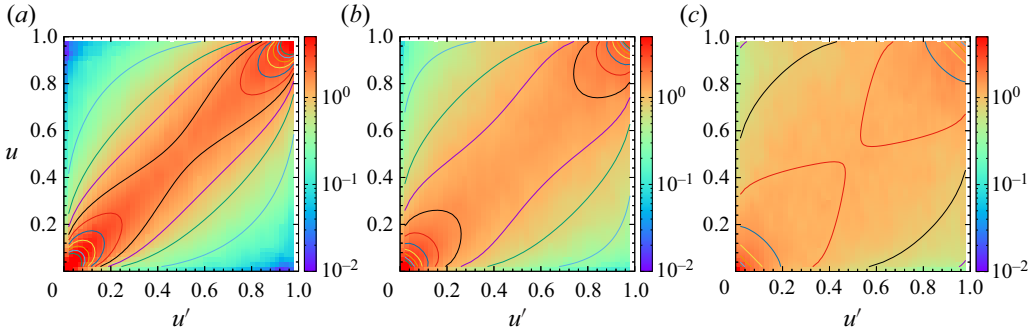
Figure 4. Empirical copulas for lag distances $\Delta s = 0.5, 1, 2$ m. The solid lines denote iso-probability lines of the stationary Gaussian copula with correlation length $\ell_c = 2.2$.

which are defined by

$$u(s) = P_s[v(s)], \quad P_s(v) = \int_0^v \mathrm{d}v' \, p_s(v'), \tag{3.6a,b}$$

where $P_s(v)$ is the cumulative distribution of $p_s(v)$. The transition probability from $u(s) = u'$ at s to $u(s + \Delta s) = u$ at $s + \Delta s$ is given by

$$c(u, \Delta s | u') = \frac{p[P_s^{-1}(u), \Delta s | P_s^{-1}(u')]}{p_s[P_s^{-1}(u)]}. \tag{3.7}$$

Analogously, the speed transition probability can be written in terms of the copula density as

$$p(v, \Delta s | v') = c[P_s(v), \Delta s | P_s(v')] \, p_s(v). \tag{3.8}$$

Figure 4 shows the empirical copula density at different lag distances Δs, which are obtained from the trajectory data as outlined in Appendix A. The data can be represented by a stationary Gaussian copula, which is characterized by the exponential correlation function $\mathcal{C}(\Delta s) = \exp(-\Delta s / \ell_c)$ and the correlation length ℓ_c; see Appendix B. The value $\ell_c = 2.2$ m fits the empirical data and is copacetic with the average fracture length.

As an immediate consequence of this finding, we note that the Gaussian copula provides an analytical model for the transition matrix in stochastic Markov models. The transition matrix can be constructed from the copula and the stationary speed distribution according to (3.8). In the following, we explore the implications of this observation further to identify the stochastic process for $v(s)$ and to derive the corresponding stochastic differential equation.

3.2.3. *Stochastic speed process*

First, we note that the fact that $\{v(s)\}$ can be described by a Gaussian copula implies that the normal score transform $w(s)$ of $v(s)$ is characterized by a multi-Gaussian distribution. The normal score transform is defined by

$$w(s) = F^{-1}[v(s)] \equiv \Phi^{-1}(p_s[v(s)]), \quad v(s) = F[w(s)] = p_s^{-1}(\Phi[w(s)]), \tag{3.9a,b}$$

where $\Phi(w)$ is the cumulative unit normal distribution. The transition probability $p_w(w, \mathrm{d}s | w')$ from $w' = w(s)$ to $w = w(s + \mathrm{d}s)$ – that is, the distribution of $w(s + \mathrm{d}s)$

977 A38-10

given that $w(s) = w'$ – is a Gaussian distribution with mean $w' \, \mathcal{C}(\mathrm{d}s) \approx w'(1 - \ell_c^{-1} \, \mathrm{d}s)$ and variance $1 - \mathcal{C}(s)^2 \approx 2\ell_c^{-1} \, \mathrm{d}s$. This implies that we can write $w(s + \mathrm{d}s)$ as

$$w(s + \mathrm{d}s) = w(s) \left(1 - \ell_c^{-1} \, \mathrm{d}s \right) + \sqrt{2\ell_c^{-1} \, \mathrm{d}s} \, \zeta(s), \tag{3.10}$$

where $\zeta(s)$ is a Gaussian random variable of zero mean and unit variance. Taking the limit $\mathrm{d}s \to 0$ in (3.10), we obtain the following stochastic differential equation for $w(s)$:

$$\frac{\mathrm{d}w(s)}{\mathrm{d}s} = -\ell_c^{-1} \, w(s) + \sqrt{2\ell_c^{-1}} \, \xi(s), \tag{3.11}$$

where $\xi(s)$ denotes a Gaussian white noise. Equation (3.11) describes an Ornstein–Uhlenbeck process, which has been used as a parsimonious model for speed series in pore-scale and Darcy-scale porous and fractured media (Morales *et al.* 2017; Hakoun, Comolli & Dentz 2019; Hyman & Dentz 2021). This indicates that the Gaussian copula structure may represent a general principle of organization of speed series in disordered media. In the following, we explore the consequences for $v(s)$ and $v(t)$ that follow from the representation of $w(s)$ as an Ornstein–Uhlenbeck process. Note that we use the same letter v for spatial and temporally variable speed. We distinguish them through their argument.

By using the Ito lemma, we obtain for $v(s) = F[w(s)]$ from (3.11) the Langevin equation

$$\frac{\mathrm{d}v(s)}{\mathrm{d}s} = -\ell_c^{-1} A[v(s)] + \sqrt{2 \, B[v(s)] \, \ell_c^{-1}} \, \xi(s), \tag{3.12}$$

where

$$A(v) = \left[-w \frac{\mathrm{d}F(w)}{\mathrm{d}w} + \frac{\mathrm{d}^2 F(w)}{\mathrm{d}w^2} \right]_{w = F^{-1}(v)}, \tag{3.13}$$

$$B(v) = \left[\frac{\mathrm{d}F(w)}{\mathrm{d}w} \right]^2_{w = F^{-1}(v)}. \tag{3.14}$$

The drift and diffusion coefficients $A(v)$ and $B(v)$ are fully defined by the Eulerian speed distribution $p_e(v)$. The initial particle velocities $v_0 = v(s = 0)$ are distributed according to $p_0(v)$, which depends on the injection condition. For uniform injection $p_0(v) = p_e(v)$, for flux-weighted injection, it is given by $p_0(v) = p_s(v)$. Thus (3.12) describes the evolution of the particle velocities for arbitrary injection conditions.

Equation (3.12) implies that the velocity distribution $p(v, s)$ evolves along a particle trajectory according to the Fokker–Planck equation

$$\frac{\partial p(v, s)}{\partial s} = -\frac{\partial}{\partial v} A(v) \, p(v, s) + \frac{\partial^2}{\partial v^2} B(v) \, p(v, s). \tag{3.15}$$

The stationary distribution $p_s(v)$ is given in terms of $A(v)$ and $B(v)$ as

$$p_s(v) = \frac{1}{B(v)} \exp \left[\int_{v_0}^{v} \mathrm{d}v' \frac{A(v')}{B(v')} \right]. \tag{3.16}$$

The integral limit v_0 is chosen such that the integral of the right-hand side is normalized to 1.

3.3. *Stochastic particle motion*

We focus on the streamwise particle motion, that is, along the direction of the mean flow velocity, which is aligned with the x-axis of the coordinate system. We project the displacement ds along the trajectory onto the streamwise displacement dx by using the advective tortuosity χ, which compares the average trajectory length to linear distance. Thus we write

$$\frac{\mathrm{d}x(s)}{\mathrm{d}s} = \frac{1}{\chi}. \tag{3.17}$$

The evolution of the particle time $t(s)$ in this framework is given by

$$\frac{\mathrm{d}t(s)}{\mathrm{d}s} = \frac{1}{v(s)}, \tag{3.18}$$

where the velocity process $v(s)$ has been defined in the previous subsection. The advective tortuosity is given by (Koponen, Kataja & Timonen 1996)

$$\chi = \frac{\langle v_e \rangle}{u_x}, \tag{3.19}$$

that is, the ratio between the average velocity magnitude and the average velocity in the primary direction of flow.

Equations (3.12)–(3.18) describe a stochastic TDRW. Particle motion is determined as a function of distance s, and time $t(s)$ is a dependent variable. The presented framework allows us to derive the equations of motion for $[x(t), v(t)]$ through the variable change d$s \to$ dt in (3.17) and (3.12), which gives

$$\frac{\mathrm{d}x(t)}{\mathrm{d}t} = \frac{v(t)}{\chi}, \tag{3.20}$$

$$\frac{\mathrm{d}v(t)}{\mathrm{d}t} = v(t)\,A[v(t)] + \sqrt{2\,v(t)\,B[v(t)]}\,\xi(t). \tag{3.21}$$

The joint p.d.f. $p(x, v, t)$ then satisfies the Klein–Kramers equation (Risken 1996)

$$\frac{\partial p(x, v, t)}{\partial t} + \frac{\partial}{\partial x}\left[\frac{v}{\chi}\,p(x, v, t)\right] = -\frac{\partial}{\partial v}v\,A(v)\,p(x, v, t) + \frac{\partial^2}{\partial v^2}v\,B(v)\,p(x, v, t). \tag{3.22}$$

This implies that the large-scale evolution of the joint p.d.f. of streamwise particle position and speed is fully defined by the Eulerian speed distribution, correlation length and tortuosity.

3.4. *Continuous time random walk*

As mentioned in the previous subsection, (3.17)–(3.18) represent a stochastic TDRW. For particle displacements $s \gg \ell_c$ much larger than the correlation length ℓ_c, the velocity process $v(s)$ can be considered as uncorrelated. Using ℓ_c as the coarse graining scale, we define $s_n = n\ell_c$, $x(s_n) = x_n$ and $v(s_n) = v_n$. With these definitions, we can discretize (3.17) and (3.18) as

$$x_{n+1} = x_n + \frac{\ell_c}{\chi}, \quad t_{n+1} = t_n + \frac{\ell_c}{v_n}. \tag{3.23a,b}$$

The recursion relations (3.23a,b) describe a CTRW (Dentz et al. 2004; Berkowitz et al. 2006) for the turning point x_n, that is, the positions at which particles change speed. Unlike

977 A38-12

for other CTRW formulations (Berkowitz *et al.* 2006), here the distribution of transition times τ_n is in general not stationary because the distribution of τ_0, the transition time for the first step, depends on the distribution of initial particle speeds, which varies according to the injection condition. This is an important feature, because large retention times in the injection region may have a strong impact on the overall plume evolution. In the following, we refer to the coarse-grained model (3.23*a,b*) as a CTRW, and the full model given by (3.17)–(3.18) as a stochastic TDRW.

The speed distributions $p_0(v)$ and $p_e(v)$ define the transition time distributions $\psi_0(t)$ for the first step and $\psi(t)$ for all following steps:

$$\psi_0(t) = \frac{\ell_c}{t^2} p_0(\ell_c/t), \quad \psi(t) = \frac{\ell_c}{t^2} p_s(v) = \frac{\ell_c^2}{t^3 v_c} p_e(\ell_c/t), \qquad (3.24a,b)$$

where we used the relation (3.5) between the steady-state speed distribution $p_s(v)$ and the Eulerian speed distribution $p_e(v)$. Unlike other CTRW formulations that assume a single transition time distribution that is fitted based on a suitable parametric function, (3.23*a,b*) provide a direct link to the underlying medium and Eulerian flow properties through the correlation length ℓ_c and the Eulerian speed distribution $p_e(v)$.

The particle distribution $p(x, t)$ satisfies

$$p(x, t) = \int_0^t dt' \, R_0(x, t') \int_{t-t'}^\infty dt'' \, \psi_0(t'') + \int_0^t dt' \, R(x, t') \int_{t-t'}^\infty dt'' \, \psi(t''), \qquad (3.25)$$

where $R_0(x, t)$ is the distribution of initial particle position and time. Here, $R(x, t)$ denotes the frequency that a particle arrives at x at time t. This equation reads as follows. The probability that a particle is at position x at time t is given by the probability that it remains at the initial position for a time larger than the current time (first term) plus the probability that it has just arrived at position x and remains there for a time larger than t (second term). Then $R(x, t)$ satisfies the equation

$$R(x, t) = \int_0^t dt' \, \psi_0(t - t') \, R_0(x - \ell_c/\chi, t') + \int_0^t dt' \, \psi(t - t') \, R(x - \ell_c/\chi, t'). \quad (3.26)$$

The first term on the right-hand side denotes the probability that the particle makes a transition from the initial position and time to (x, t), while the second term denotes the probability that the particle makes a transition from any other possible position and time to (x, t).

Combination of the Laplace transforms of (3.25) and (3.26) to eliminate $R^*(x, \lambda)$ gives for $p^*(x, \lambda)$ the equation

$$\lambda p^*(x, \lambda) = R_0(x, \lambda) - \frac{\psi^*(\lambda) - \psi_0^*(\lambda)}{1 - \psi^*(\lambda)} \left[R_0^*(x - \ell_c/\chi, \lambda) - R_0^*(x, \lambda) \right]$$
$$+ \frac{\lambda \, \psi^*(\lambda)}{1 - \psi^*(\lambda)} \left[p^*(x - \ell_c/\chi, \lambda) - p^*(x, \lambda) \right]. \qquad (3.27)$$

The Laplace transform is defined in Abramowitz & Stegun (1972). Laplace transformed quantities are marked by an asterisk, and the Laplace variable is denoted by λ. For $\psi_0(t) \equiv \psi(t)$, (3.27) is equal to the generalized master equation (Berkowitz *et al.* 2006). Note that (3.27) represents the coarse-grained projection of the Klein–Kramers equation (3.22) from (x, v)-space to x-space. The coarse-grained formulation of the stochastic

TDRW as a CTRW allows us to obtain relatively compact Laplace-space expressions for the distribution of first passage times and the displacement moments, and facilitates the analytical prediction of their long-time scaling. The emphasis here is on the dependence of the long-time behaviour on the initial velocity distribution and thus the injection conditions, which have not been studied with other CTRW formulations.

3.4.1. *First passage time distributions*

The first passage times at linear distance x_n are given by t_n, where $n = \inf(n|x_n \geq x)$, that is,

$$t_n = \sum_{j=0}^{n-1} \frac{\ell_c}{v_j}. \tag{3.28}$$

The distribution $f_n(t)$ of first passage times is given by $f_n(t) = \langle \delta[t - t_n] \rangle$. It can be written in Laplace space as

$$f_n^*(\lambda) = \psi_0^*(\lambda)\,\psi^*(\lambda)^{n_c-1} = \exp\left(\ln[\psi_0^*(\lambda)] + (n_c - 1)\ln[\psi^*(\lambda)]\right). \tag{3.29}$$

3.4.2. *Displacement mean and variance*

In order to determine the displacement mean and variance, we use the Fourier transform $\tilde{p}^*(k, \lambda)$ of $p^*(x, \lambda)$. It satisfies

$$\lambda\tilde{p}^*(k, \lambda) = 1 - \frac{\psi^*(\lambda) - \psi_0^*(\lambda)}{1 - \psi^*(\lambda)}\,[\exp(\mathrm{i}k\ell_c/\chi) - 1]$$
$$+ \frac{\lambda\,\psi^*(\lambda)}{1 - \psi^*(\lambda)}\,\tilde{p}^*(k, \lambda)\,[\exp(\mathrm{i}k\ell_c/\chi) - 1], \tag{3.30}$$

where we set $R_0^*(x, \lambda) = \delta(x)$. The Fourier transform pair of a function $\varphi(x)$ is here defined by

$$\tilde{\varphi}(k) = \int_{-\infty}^{\infty} \mathrm{d}x \exp(\mathrm{i}kx)\,\varphi(x), \quad \varphi(x) = \int_{-\infty}^{\infty} \frac{\mathrm{d}k}{2\pi} \exp(-\mathrm{i}kx)\,\tilde{\varphi}(k), \tag{3.31a,b}$$

with wavenumber denoted by k. We obtain from (3.30) for $\tilde{p}^*(k, \lambda)$ that

$$\tilde{p}^*(k, \lambda) = \frac{1}{\lambda} \frac{1 + \dfrac{\Delta\psi^*(\lambda)}{1 - \psi^*(\lambda)}\,\mathcal{F}(k)}{1 - \dfrac{\psi^*(\lambda)}{1 - \psi^*(\lambda)}\,\mathcal{F}(k)}, \tag{3.32}$$

where we defined

$$\mathcal{F}(k) = \exp(\mathrm{i}k\ell_c/\chi) - 1, \quad \Delta\psi^*(\lambda) = \psi_0^*(\lambda) - \psi^*(\lambda). \tag{3.33a,b}$$

The Laplace transform of the nth displacement moment is given in terms of $\tilde{p}^*(k, \lambda)$ as

$$m_n^*(\lambda) = (-\mathrm{i})^n \left.\frac{\partial \tilde{p}^*(k, \lambda)}{\partial k}\right|_{k=0}. \tag{3.34}$$
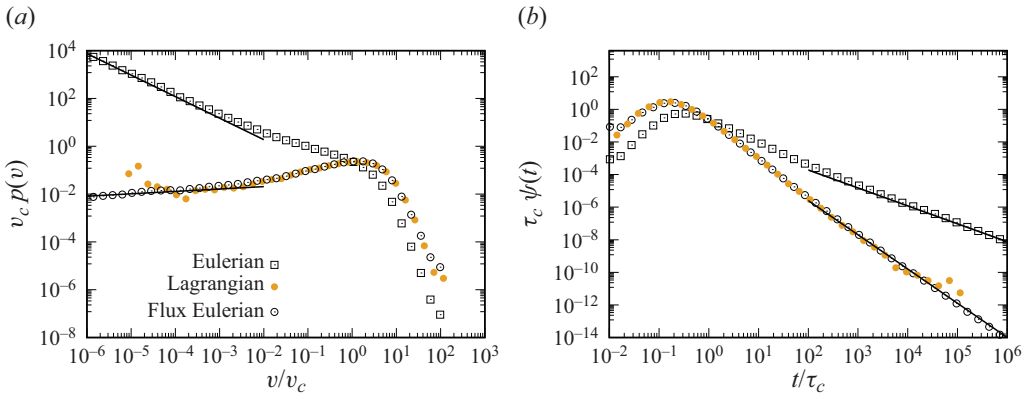
Figure 5. (*a*) Eulerian speed distribution $p_e(v)$, flux-weighted speed distribution and stationary Lagrangian speed distribution $p_s(v)$. The solid lines denote the scalings $v^{\beta-1}$ and v^β with $\beta = 0.1$. (*b*) Corresponding transition time distributions. The solid lines denote the scalings $t^{-1-\beta}$ and $t^{-2-\beta}$.

The zeroth moment is 1 by definition because of the normalization of the particle distribution. The first and second moments are given by

$$m_1^*(\lambda) = \frac{1}{\lambda} \frac{\ell_c}{\chi} \frac{\psi_0^*(\lambda)}{1 - \psi^*(\lambda)}, \tag{3.35}$$

$$m_2^*(\lambda) = \frac{1}{\lambda} \frac{\ell_c^2}{\chi^2} \left[\frac{\psi_0^*(\lambda)}{1 - \psi^*(\lambda)} + 2 \frac{\psi^*(\lambda)\,\psi_0^*(\lambda)}{[1 - \psi^*(\lambda)]^2} \right]. \tag{3.36}$$

The displacement variance is given by

$$\sigma^2(t) = m_2(t) - m_1(t)^2. \tag{3.37}$$

4. Transport behaviours

In this section, we use the stochastic theory developed in the previous section to analyse the flow and transport behaviours obtained from the detailed numerical simulations described in § 2.5 and gain insight into the mechanisms of large-scale solute transport in fractured media. We first analyse the predicted speed statistics. Then we focus on arrival time distributions and displacement moments.

4.1. *Speed statistics and transition times*

Figure 5 shows the distribution $p_e(v)$ of Eulerian flow speeds and the Lagrangian speed distribution $p_s(v)$. The mean flow speed is $v_c = 357 \text{ m yr}^{-1}$. According to the theory, they are related by (3.5) through flux-weighting. This relation is confirmed by the numerical data presented in the figure. Furthermore, we observe that the behaviour of $p_e(v)$ at low flow speeds $v < 10^{-3} v_c$ can be approximated by the power law $p_e(v) \sim v^{\beta-1}$ with $\beta = 0.1$. The high frequency of small flow speeds is remarkable given the relative regularity of the fracture network, which is characterized by constant fracture aperture, constant fracture length, but variable orientation; see § 2.1. Thus this broad distribution of flow speeds is due to the geometrical disorder of the fracture network. Current approaches to link flow speed

and network characteristics are based on the Poiseuille law to link aperture distribution and speed. Such approaches do not apply here because the aperture is constant.

The transition time distributions $\psi_0(t)$ and $\psi(t)$ corresponding to $p_e(v)$ and $p_s(v)$ are shown in figure 5(*b*). The characteristic transition time is $\tau_c = \ell_c/v_c$. The transition time distribution $\psi(t)$ scales as $t^{-2-\beta}$ for $t \gg \tau_c$. This implies for its Laplace transform $\psi^*(\lambda)$ the behaviour

$$\psi^*(\lambda) = 1 - \lambda\tau_c + a(\lambda\tau_c)^{\beta+1}, \tag{4.1}$$

for $\lambda\tau_c \gg 1$, where a is a constant, and the characteristic time τ_c is equal to the mean transition time. The transition time $\psi_0(t)$ for the initial step scales as $t^{-1-\beta}$ for $t\tau_c$. This implies for its Laplace transform that

$$\psi_0^*(\lambda) = 1 - a_0(\lambda\tau_c)^\beta, \tag{4.2}$$

where a_0 is a constant.

4.2. *First passage time distributions*

Figure 6 shows the first passage time distribution (*fptd*) at different distances $x = 10$, 40, 100 and 1000 m from the inlet plane. We observe tailing for both injection conditions. For the uniform injection, tailing is much stronger, i.e. slower decay, than for flux-weighted. Recall that the difference between the uniform and flux-weighted injection is the relative increase of particles in low-flow regions for uniform compared to flux-weighted injection. Thus stronger retention of particles at the inlet plane for uniform injection causes the broadening of the first passage time distribution towards long times. The stochastic TDRW model predicts accurately both the peak and tail behaviours for uniform and flux-weighted injection, and thus seems to capture the correct large-scale propagator of the complex flow and transport system. The late-time behaviour for the uniform injection is characterized by the power-law scaling $t^{-1-\beta}$. For the flux-weighted injection, the tails scale as $t^{-2-\beta}$. This latter scaling is a consequence of the generalized central limit theorem. In fact, the arrival time distribution converges towards a stable distribution with distance from the inlet (Hyman *et al.* 2019*a*).

For the convenience of the reader, we summarize the main arguments in the following. We start from (2.9) for the Laplace transform of the arrival time distribution in the equivalent CTRW. For the flux-weighted injection, we can write for $\lambda\tau_c \gg 1$ that

$$f_n^*(\lambda) = \exp\left(-\langle t_n\rangle\lambda\right) g_n^*[\lambda\langle t_n\rangle^{1/(1+\beta)}], \tag{4.3}$$

where we defined

$$g_n^*(\lambda) = \exp\left[\frac{a}{\tau_c}(\lambda\tau_c)^{1+\beta} + \cdots\right]. \tag{4.4}$$

Note that $\langle t_n\rangle = n\tau_c$. To arrive at (4.3), we used (4.1) for the Laplace transform $\psi^*(\lambda)$ of $\psi(t)$, and Taylor expanded the logarithm in (2.9). The dots in (4.4) denote contributions that go to zero in the limit $n \to \infty$ (Hyman *et al.* 2019*a*). Thus $\lim_{n\to\infty} g_n(\lambda) = g_\beta^*(\lambda)$, where $g_\beta^*(\lambda) = \exp[a(\lambda\tau_c)/\tau_c]$ is a stable density that is totally skewed to the right. This
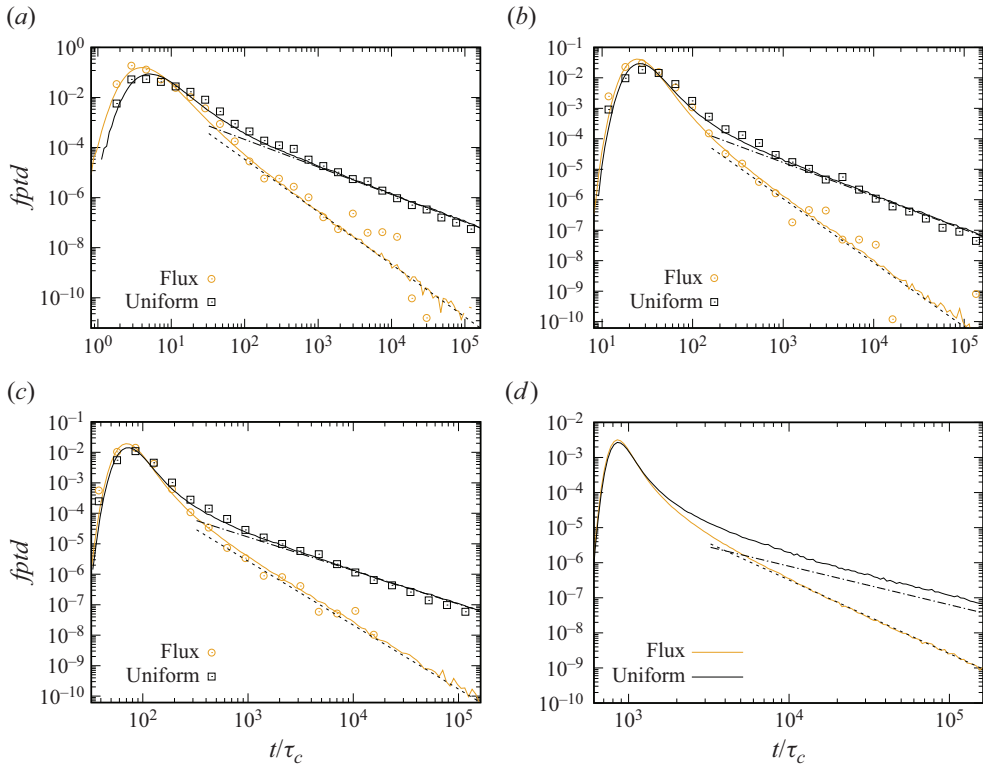
Figure 6. Arrival time distributions at distances (top left to bottom right) $x = 10, 40, 100, 1000$ m from the inlet. Symbols correspond to the numerical simulations, and solid lines to the stochastic TDRW model for (orange) flux-weighted and (black) uniform injection. The dash-dotted lines indicate the scaling $t^{-1-\beta}$, and the dashed lines indicate the scaling $t^{-2-\beta}$, with $\beta = 0.1$.

implies that for large $n, f_n(t)$ tends towards the scaling form:

$$f_n(t) \rightarrow \frac{g_\beta[(t - \langle t_n \rangle)/\langle t_n \rangle^{1/(1+\beta)}]}{\langle t_n \rangle^{1/(1+\beta)}}. \tag{4.5}$$

Figure 7 illustrates the tail behaviours for flux-weighted injection at different distances. They collapse on the same curve when rescaled appropriately, according to their stable limit.

This is different for the uniform injection. We see from figure 6 that the peak behaviours of the flux-weighted and uniform injections converge with increasing distance from the inlet. The tail behaviour, however, is distinctly different, characterized by different exponents. Moreover, the tails collapse on the same curve. This is emphasized in figure 7, in which the arrival time distributions for uniform injection are rescaled according to (4.5). The peak behaviours are similar to those for the flux-weighted injection, and seem to converge to the stable form. The tails of the rescaled arrival time distributions do not collapse onto a single curve. Thus there seems to be convergence in the bulk, but not in the tails of the distribution. This behaviour can be explained by inspecting again (2.9), which now can be written as

$$f_n^*(\lambda) = \psi_0^*(\lambda) \exp\left(-\langle t_{n-1} \rangle \lambda\right) g_{n-1}[\lambda \langle t_{n-1} \rangle^{1/(1+\beta)}], \tag{4.6}$$
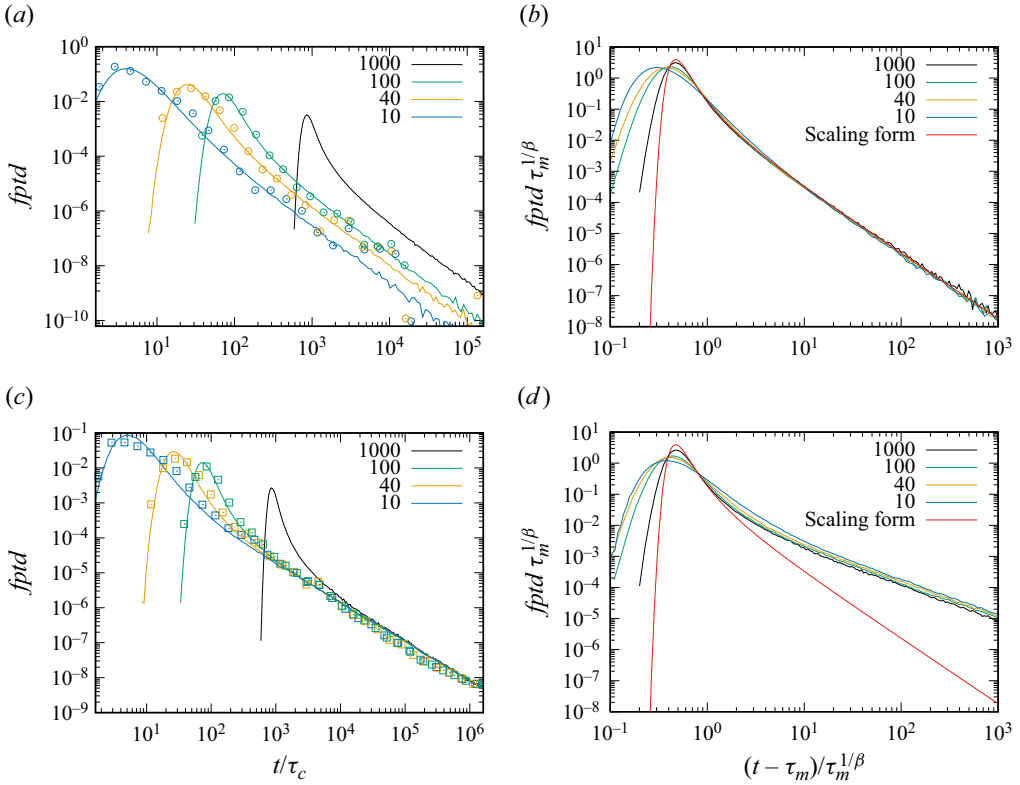
977 A38-17

Figure 7. Arrival time distributions for (*a*) flux-weighted and (*b*) uniform injection at distances $x = 10, 40, 100, 1000$ m from the inlet from (symbols) numerical simulations and (solid lines) the stochastic TDRW model. The black solid line denotes the prediction of the stochastic TDRW model for $x = 1000$ m. (*b,d*) The same data as in corresponding panels (*a,c*) rescaled according to (4.3). The red lines denote the scaling form given by (4.5). Note that we display only the data from the stochastic TDRW model, which are sufficient due to the agreement with the data from the numerical simulations shown in (*a,c*).

where $\langle t_{n-1} \rangle = (n-1)\tau_c$. Thus, in the limit of $n \gg 1$, the arrival time distribution can be written as

$$f_n(t) = \int_0^t dt' \, \psi_0(t - t') \frac{g_\beta[(t' - \langle t_n \rangle)/\langle t_n \rangle^{1/(1+\beta)}]}{\langle t_n \rangle^{1/(1+\beta)}}. \tag{4.7}$$

It is the convolution of the initial transition time distribution with the stable distribution. The long-time tail is due to the first time step, which all arrival time distributions have in common. Therefore, the tails collapse on the same curve. The peak behaviour, on the other hand, stems from the summation of transition times that are distributed according to $\psi(t)$. This explains the convergence of the peak behaviour to the peak of the stable law. In summary, the bulk of the arrival time distribution converges to a stable law, and the tail retains the memory of the velocity at the injection plane.

4.3. *Displacement mean and variance*

Figure 8 shows the displacement mean and variance for uniform and flux-weighted injections. The observation times are smaller than the time when the first particles leave the
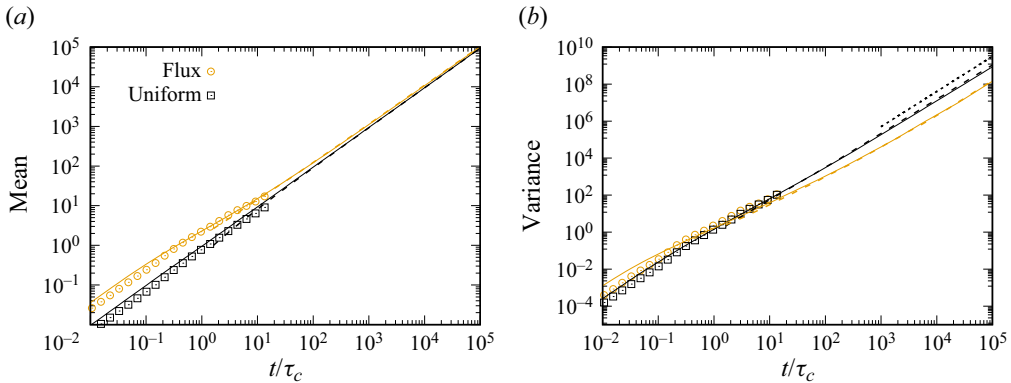
977 A38-18

Figure 8. Displacement (*a*) mean and (*b*) variance from (symbols) numerical simulations and (solid lines) the stochastic TDRW model for (orange) flux-weighted and (black) uniform injection. The dashed lines show the long-time predictions of the CTRW model described in § 3.4. The dotted line indicates the power-law behaviour (4.11).

domain. Due to the occurrence of fast pathways, this time is relatively short. The upscaled theory reproduces the evolution of the displacement mean for both injection conditions.

The early-time behaviour of the mean displacement is given by

$$m_1(t) = \langle v_0 \rangle t / \chi, \tag{4.8}$$

where $\langle v_0 \rangle$ is the mean initial speed. Its asymptotic long-time behaviour is

$$m_1(t) = v_c t / \chi, \tag{4.9}$$

because the temporal speed statistics asymptote towards $p_e(v)$. The displacement variance at early times shows ballistic behaviour, which is due to the persistence of the initial velocities,

$$\sigma^2(t) = \frac{\sigma_{v_0}^2}{\chi^2} t^2, \tag{4.10}$$

where $\sigma_{v_0}^2$ is the variance of the initial speed distribution $p_0(v)$. After the ballistic early-time regime, the variances cross over to a power-law regime that is determined by the exponent β that determines the behaviour of $p_e(v)$ at $v \ll v_c$; see figure 5. From the explicit Laplace space expressions (3.35) and (3.36), we can derive the following asymptotic expressions for the uniform and flux-weighted initial conditions:

$$\sigma^2(t) = \frac{v_c^2}{\chi^2} t^{2-\alpha} \frac{2\alpha a + 2a_0(1-\alpha)}{\Gamma(3-\alpha)}, \tag{4.11}$$

$$\sigma^2(t) = \frac{v_c^2}{\chi^2} t^{2-\alpha} \frac{2\alpha a}{\Gamma(3-\alpha)}, \tag{4.12}$$

respectively. We used expressions (4.1) and (4.2).

For the uniform injection, the temporal velocity statistics are stationary; see § 3.2. Therefore, as shown in figure 8, the mean transport speed is equal to the Eulerian mean speed $v_c = \langle v_e \rangle$, and the displacement mean evolves linearly with time according to (4.9). The numerical early-time data are slightly below the model prediction. This is due to

the fact that the initial speed distribution $p_0(v)$ deviates from $p_e(v)$ at high speeds, as shown in figure 2, which implies that the initial mean speed is smaller than $\langle v_e \rangle$. A similar behaviour is observed for the flux-weighted injection, for which the theory predicts the early-time behaviour $m_1(t) = v_f t / \chi$, where v_f denotes the mean of $p_s(v)$. It is given by $v_f = \langle v_e^2 \rangle / \langle v_e \rangle$, where $\langle v_e^2 \rangle$ is the mean squared Eulerian flow speed. Here as well, the numerical data are slightly below the model prediction. For both injection modes, the mean displacements converge for times $t \gg \tau_c$ because the temporal velocity statistics asymptote towards $p_e(v)$.

As outlined above, the early-time behaviour of the displacement variance is ballistic, characterized by the initial speed variance. Also here, the model prediction slightly overestimates the numerical data; see figure 8. The variance for the flux-weighted injection is initially larger than for the uniform injection because of the higher initial speed variance. Then for times larger than the mean advection time τ_c, it slows down and remains at smaller values than for the uniform injection. The long-time evolution for both injection conditions is characterized by the power-law behaviour predicted in (4.11). At times $t \gg \tau_c$, the variance for the uniform injection grows faster than for the flux-weighted injection because there is a a stronger temporal persistence of lower velocities. The persisting contrast between slow particles and fast particles leads to faster growth.

The theoretical model captures the early-time behaviour of tracer displacement and dispersion, and predicts anomalous dispersion at large times caused by the broad distribution of flow speeds. The asymptotic dispersion behavior and the difference between injection conditions is also captured by the proposed CTRW model that accounts for arbitrary initial transition time distributions.

5. Summary and conclusions

We study the upscaling and prediction of large-scale transport in three-dimensional random fracture networks. To this end, we analyse particle trajectories and speed data from detailed numerical flow and particle tracking simulations. Unlike classical approaches, Lagrangian statistics are sampled equidistantly along trajectories, instead of at constant rate. This sampling strategy accounts for the fact that Lagrangian velocities vary on the spatial scales imprinted in the fracture network. The statistics of the resulting speed series are quantified in terms of the transition probability of subsequent speeds at different lag distances and the stationary speed distribution. In order to characterize their correlation structure, we determine the copula densities corresponding to the transition probabilities. The correlation structure can be described by a stationary Gaussian copula. This renders an analytical model for the transition probabilities, which can be constructed as the product of the copula and the stationary speed distribution. Moreover, this result implies directly that the normal score transforms of equidistant particle speeds evolve as an Ornstein–Uhlenbeck process. The speed series then describes a stationary Markov process that is defined uniquely by its stationary distribution and the correlation length. The former is given by the flux-weighted Eulerian speed distribution; the latter is determined by the average fracture length, which sets the characteristic distance for speed transitions. The resulting upscaled transport model can be contextualized as a stochastic time-domain random walk (TDRW) because it describes particle motion through equidistant transitions in space combined with a kinematic transition time that is inversely proportional to the evolving particle speed. It is predictive in the sense that it can be parametrized in terms of transport-independent attributes.

Based on this formulation, we derive the stochastic evolution equation for Lagrangian particle speeds both in space and in time, and show that the stochastic particle dynamics are equivalent to a Klein–Kramers equation for the temporal evolution of the joint distribution of particle position and speed. For transition lengths of the order of the correlation length of particle speeds – that is, if subsequent speeds are statistically independent – particle motion can be coarse-grained as a continuous time random walk (CTRW). These upscaled stochastic models allow for the prediction of longitudinal dispersion based only on medium and flow properties, that is, the average fracture length, the Eulerian speed distribution, and advective tortuosity. The prediction of transport, in terms of the spatial network structure and flow boundary conditions only, remains an open question. However, in the proposed framework, this question is reduced to finding a map between medium structure and Eulerian flow distribution.

The resulting models are used to interpret the transport behaviours obtained from detailed numerical simulations in a single realization of a random fracture network. We focus on first passage time distributions at control planes at different distances from the inlet plane, and the temporal evolution of displacement mean and variance, for both flux-weighted and uniform particle injections. The presented theory predicts that the spatial speed statistics are stationary under flux-weighted injection, and the temporal statistics under uniform injection. This is confirmed by the numerical data. The first passage time distributions show distinctly different long-time scalings for uniform and flux-weighted injections. Both are characterized by power-law decay, albeit at different exponents, which differ by 1. The theory links the observed behaviours directly to the Eulerian speed distribution and injection conditions. It shows that the first passage time distribution for the flux-weighted injection evolves towards a stable law, while for the uniform injection, it is given by the convolution of the initial transit time and the stable distribution for flux-weighted injection. That is, it converges in the bulk towards a stable distribution, while the memory of the initial condition persists in the tail. Similarly, for the displacement mean and variance, we observe different behaviours depending on the initial conditions. Unlike for the arrival time distributions, here, the asymptotic scalings are the same for both injection modes. Through their explicit dependence on the initial speed distribution, the presented TDRW and CTRW models allow us to link observed tracer data to the injection or source conditions.

Note that the model medium represents a generic disordered fracture network composed of a single family of monodisperse fractures, which gives rise to a single characteristic length scale, the mean fracture length. In geological media, also networks with multiple fracture families whose lengths follow truncated power-law distributions are commonly observed Bonnet *et al.* (2001). For broad distributions of fracture lengths, one does not expect the spatially sampled velocity process to be Markovian. In this case, a different sampling strategy needs to be employed that renders the velocity process of short memory. A possible sampling variable could be the number of fractures passed by a particle. The generalization of the proposed framework for this type of networks is currently under investigation.

Considering the impact of different fracture orientations on large-scale transport, they are important only in regard to their arrangement relative to the primary driving force. Fracture orientations impact on the correlation length and Eulerian velocity distributions, which are the only inputs for the proposed models. Thus this network characteristic can be represented implicitly in the framework of the presented TDRW and CTRW models.

In conclusion, the proposed theory is able to capture and predict the evolution of the observed non-Fickian transport behaviours for arbitrary initial speed distributions. We

have seen that this is a key feature for the prediction of the early-time but also late-time behaviours if the initial conditions impart a long memory. The coarse graining of the stochastic TDRW model using the mean fracture length gives a CTRW. However, unlike current CTRW formulations, the derived model is conditioned on the initial transition time distribution, which in general is different from the steady-state distribution. These models can be fully parametrized by the pointwise Eulerian flow statistics and the characteristic fracture length, both of which are not transport attributes. Thus they overcome a common criticism of CTRW-based approaches, which are often descriptive with a parametrization that is based on transport data. These findings enable a predictive theory for large-scale transport in random fracture networks.

Author ORCIDs.
Marco Dentz https://orcid.org/0000-0002-3940-282X.

Appendix A. Speed copula

To characterize empirically the conditional p.d.f. $p(v, \Delta s|v')$ of subsequent particle speeds separated by Δs, the velocity space is discretized into N bins $B_1, \ldots, B_N$ with $B_j = (v_j, v_{j+1}]$. The probability P_j of $v(s)$ being in bin B_j is

$$P_j \equiv \mathrm{Prob}[v(s) \in B_j]$$
$$= P_s(v_{j+1}) - P_s(v_j) = \int_{v_j}^{v_{j+1}} \mathrm{d}v \, p_s(v), \tag{A1}$$

where $P_s(v) \in [0, 1]$ is the cumulative speed distribution. In order to characterize velocity transitions, we employ the joint distribution P_{ij} of $v(s + \Delta s)$ being in bin B_i and $v(s)$ in bin B_j:

$$P_{ij} = \int_{v_i}^{v_{i+1}} \mathrm{d}v \int_{v_j}^{v_{j+1}} \mathrm{d}v' \, p(v, \Delta s, v'), \tag{A2}$$

where $p(v, \Delta s, v')$ is the joint p.d.f. of $v(s)$ and $v(s + \Delta s)$. Velocity transitions are quantified by the transition matrix

$$T_{ij} = \frac{P_{ij}}{P_j}, \tag{A3}$$

where the joint and marginal distributions P_{ij} and P_j are obtained by sampling speeds along and between trajectories as

$$P_{ij} = \frac{1}{n_t} \sum_{k=1}^{n_t} \frac{1}{L_k} \int_0^{L_k} ds \, \mathbb{I} \left[v_k(s + \Delta s) \in B_i \wedge v_k(s) \in B_j \right], \tag{A4}$$

$$P_j = \frac{1}{n_t} \sum_{k=1}^{n_t} \frac{1}{L_k} \int_0^{L_k} ds \, \mathbb{I} \left[v_k(s) \in B_j \right], \tag{A5}$$

where n_t is the number of trajectories, and L_k is the length of the kth trajectory. The numerical single point and conditional speed p.d.f.s are approximated by

$$p(v_i) = \frac{P_i}{B_i}, \quad p(v_i, \Delta s | v_j) = \frac{T_{ij}}{B_i}. \tag{A6a,b}$$

In order to determine the empirical copula density, we use equiprobable bins, i.e. $P_j = 1/N$, and define

$$u_j = \sum_{k=1}^{j} P_k = \frac{j}{N}, \quad \Delta u = \frac{1}{N}. \tag{A7a,b}$$

The joint distribution density of u_i and u_j is then

$$c(u_i, \Delta s, u_j) = \frac{P_{ij}}{\Delta u^2} = N^2 P_{ij}. \tag{A8}$$

According to (A4), $c(u_i, \Delta s, u_j)$ can be sampled directly from $\{v(s)\}$ as

$$c(u_i, \Delta s | u_j) = \frac{N^2}{n_t} \sum_{k=1}^{n_t} \frac{1}{L_k} \int_0^{L_k} ds \, \mathbb{I} \left[v_k(s + \Delta s) \in B_i \wedge v_k(s) \in B_j \right]. \tag{A9}$$

Appendix B. Gaussian copula

The stationary Gaussian copula is defined by

$$c(u, s; u') = \frac{\exp \left[-\dfrac{\Phi^{-1}(u)^2 \, \mathcal{C}(s)^2 + \Phi^{-1}(u')^2 \, \mathcal{C}(s)^2 - 2\Phi^{-1}(u) \, \Phi^{-1}(u') \, \mathcal{C}(s)}{2(1 - \mathcal{C}(s)^2)} \right]}{\sqrt{1 - \mathcal{C}(s)^2}}, \tag{B1}$$

where

$$\Phi(w) = \frac{1}{2} \left[\text{erf} \left(\frac{w}{\sqrt{2}} \right) + 1 \right], \tag{B2}$$

$$\Phi^{-1}(u) = \sqrt{2} \, \text{erf}^{-1}(2u - 1), \tag{B3}$$

with $\text{erf}^{-1}(u)$ the inverse error function. Stationarity implies that the correlation function $\mathcal{C}(s)$ is exponential,

$$\mathcal{C}(s) = \exp(-s/\ell_c). \tag{B4}$$

REFERENCES

ABRAMOWITZ, M. & STEGUN, I.A. 1972 *Handbook of Mathematical Functions*. Dover Publications.

BATCHELOR, G.K. 2000 *An Introduction to Fluid Dynamics*. Cambridge University Press.

BECKER, M.W. & SHAPIRO, A.M. 2000 Tracer transport in fractured crystalline rock: evidence of nondiffusive breakthrough tailing. *Water Resour. Res.* **36** (7), 1677–1686.

BENKE, R. & PAINTER, S. 2003 Modeling conservative tracer transport in fracture networks with a hybrid approach based on the Boltzmann transport equation. *Water Resour. Res.* **39** (11), 1324.

BERKOWITZ, B., CORTIS, A., DENTZ, M. & SCHER, H. 2006 Modeling non-Fickian transport in geological formations as a continuous time random walk. *Rev. Geophys.* **44** (2).

BERKOWITZ, B. & SCHER, H. 1997 Anomalous transport in random fracture networks. *Phys. Rev. Lett.* **79** (20), 4038.

BERRE, I., DOSTER, F. & KEILEGAVLEN, E. 2019 Flow in fractured porous media: a review of conceptual models and discretization approaches. *Trans. Porous Med.* **130**, 215–236.

BODIN, J., POREL, G. & DELAY, F. 2003 Simulation of solute transport in discrete fracture networks using the time domain random walk method. *Earth Planet. Sci. Lett.* **208** (3–4), 297–304.

BONNET, E., BOUR, O., ODLING, N.E., DAVY, P., MAIN, I., COWIE, P. & BERKOWITZ, B. 2001 Scaling of fracture systems in geological media. *Rev. Geophys.* **39** (3), 347–383.

CARRERA, J., SÁNCHEZ-VILA, X., BENET, I., MEDINA, A., GALARZA, G.A. & GUIMERÁ, J. 1998 On matrix diffusion: formulations, solution methods and qualitative effects. *Hydrogeol. J.* **6**, 178–190.

COMOLLI, A., HAKOUN, V. & DENTZ, M. 2019 Mechanisms, upscaling, and prediction of anomalous dispersion in heterogeneous porous media. *Water Resour. Res.* **55** (10), 8197–8222.

DE ANNA, P., LE BORGNE, T., DENTZ, M., TARTAKOVSKY, A.M., BOLSTER, D. & DAVY, P. 2013 Flow intermittency, dispersion, and correlated continuous time random walks in porous media. *Phys. Rev. Lett.* **110** (18), 184502.

DELAY, F. & BODIN, J. 2001 Time domain random walk method to simulate transport by advection–dispersion and matrix diffusion in fracture networks. *Geophys. Res. Lett.* **28** (21), 4051–4054.

DEMMY, G., BERGLUND, S. & GRAHAM, W. 1999 Injection mode implications for solute transport in porous media: analysis in a stochastic Lagrangian framework. *Water Resour. Res.* **35** (7), 1965–1973.

DENTZ, M., CORTIS, A., SCHER, H. & BERKOWITZ, B. 2004 Time behavior of solute transport in heterogeneous media: transition from anomalous to normal transport. *Adv. Water Resour.* **27** (2), 155–173.

DENTZ, M., KANG, P., COMOLLI, A., LE BORGNE, T. & LESTER, D.R. 2016 Continuous time random walks for the evolution of Lagrangian velocities. *Phys. Rev. Fluids* **1** (7), 074004.

DREYBRODT, W., GABROVŠEK, F. & ROMANOV, D. 2005 *Processes of Speleogenessis: A Modeling Aproach*, vol. 4. Založba ZRC.

FRAMPTON, A. & CVETKOVIC, V. 2009 Significance of injection modes and heterogeneity on spatial and temporal dispersion of advecting particles in two-dimensional discrete fracture networks. *Adv. Water Resour.* **32** (5), 649–658.

FRAMPTON, A. & CVETKOVIC, V. 2011 Numerical and analytical modeling of advective travel times in realistic three-dimensional fracture networks. *Water Resour. Res.* **47** (2), W02506.

GEIGER, S., CORTIS, A. & BIRKHOLZER, J.T. 2010 Upscaling solute transport in naturally fractured porous media with the continuous time random walk method. *Water Resour. Res.* **46**, W12530.

GOEPPERT, N., GOLDSCHEIDER, N. & BERKOWITZ, B. 2020 Experimental and modeling evidence of kilometer-scale anomalous tracer transport in an alpine karst aquifer. *Water Res.* **178**, 115755.

GOTOVAC, H., CVETKOVIC, V. & ANDRICEVIC, R. 2009 Flow and travel time statistics in highly heterogeneous porous media. *Water Resour. Res.* **45** (7), W07402.

GOTOVAC, H., CVETKOVIC, V. & ANDRICEVIC, R. 2010 Significance of higher moments for complete characterization of the travel time probability density function in heterogeneous porous media using the maximum entropy principle. *Water Resour. Res.* **46** (5), W05502.

HADGU, T., KARRA, S., KALININA, E., MAKEDONSKA, N., HYMAN, J.D., KLISE, K., VISWANATHAN, H.S. & WANG, Y. 2017 A comparative study of discrete fracture network and equivalent continuum models for simulating flow and transport in the far field of a hypothetical nuclear waste repository in crystalline host rock. *J. Hydrol.* **553**, 59–70.

HAGGERTY, R., FLEMING, S.W., MEIGS, L.C. & MCKENNA, S.A. 2001 Tracer tests in a fractured dolomite 2. Analysis of mass transfer in single-well injection-withdrawal tests. *Water Resour. Res.* **37**, 1129–1142.

HAGGERTY, R. & GORELICK, S.M. 1995 Multiple-rate mass transfer for modeling diffusion and surface reactions in media with pore-scale heterogeneity. *Water Resour. Res.* **31**, 2383–2400.

HAKOUN, V., COMOLLI, A. & DENTZ, M. 2019 Upscaling and prediction of Lagrangian velocity dynamics in heterogeneous porous media. *Water Resour. Res.* **55**, 3976–3996.

HASLAUER, C.P., BÁRDOSSY, A. & SUDICKY, E.A. 2017 Detecting and modelling structures on the micro and the macro scales: assessing their effects on solute transport behaviour. *Adv. Water Resour.* **107**, 439–450.

HYMAN, J.D. & DENTZ, M. 2021 Transport upscaling under flow heterogeneity and matrix-diffusion in three-dimensional discrete fracture networks. *Adv. Water Resour.* **155**, 103994.

HYMAN, J.D., DENTZ, M., HAGBERG, A. & KANG, P. 2019*a* Emergence of stable laws for first passage times in three-dimensional random fracture networks. *Phys. Rev. Lett.* **123** (24), 248501.

HYMAN, J.D., DENTZ, M., HAGBERG, A. & KANG, P. 2019*b* Linking structural and transport properties in three-dimensional fracture networks. *J. Geophys. Res.: Sol. Ea.* **124**, 1185–1204.

HYMAN, J.D., GABLE, C.W., PAINTER, S.L. & MAKEDONSKA, N. 2014 Conforming Delaunay triangulation of stochastically generated three dimensional discrete fracture networks: a feature rejection algorithm for meshing strategy. *SIAM J. Sci. Comput.* **36** (4), A1871–A1894.

HYMAN, J.D. & JIMÉNEZ-MARTÍNEZ, J. 2017 Dispersion and mixing in three-dimensional discrete fracture networks: nonlinear interplay between structural and hydraulic heterogeneity. *Water Resour. Res.* **54** (5), 3243–3258.

HYMAN, J.D., JIMÉNEZ-MARTÍNEZ, J., GABLE, C.W., STAUFFER, P.H. & PAWAR, R.J. 2019*c* Characterizing the impact of fractured caprock heterogeneity on supercritical CO_2 injection. *Trans. Porous Med.* **131**, 935–955.

HYMAN, J.D., PAINTER, S.L., VISWANATHAN, H., MAKEDONSKA, N. & KARRA, S. 2015 Influence of injection mode on transport properties in kilometer-scale three-dimensional discrete fracture networks. *Water Resour. Res.* **51** (9), 7289–7308.

HYMAN, J.D., RAJARAM, H., SRINIVASAN, S., MAKEDONSKA, N., KARRA, S., VISWANATHAN, H. & SRINIVASAN, G. 2019*d* Matrix diffusion in fractured media: new insights into power law scaling of breakthrough curves. *Geophys. Res. Lett.* **46** (23), 13785–13795.

JANKOVIĆ, I. & FIORI, A. 2010 Analysis of the impact of injection mode in transport through strongly heterogeneous aquifers. *Adv. Water Resour.* **33** (10), 1199–1205.

DE JOSSELIN DE JONG, G. 1958 Longitudinal and transverse diffusion in granular deposits. *Trans. Am. Geophys. Un.* **39**, 67–74.

KANG, P.K., DENTZ, M., LE BORGNE, T. & JUANES, R. 2011 Spatial Markov model of anomalous transport through random lattice networks. *Phys. Rev. Lett.* **107**, 180602.

KANG, P.K., DENTZ, M., LE BORGNE, T., LEE, S. & JUANES, R. 2017 Anomalous transport in disordered fracture networks: spatial Markov model for dispersion with variable injection modes. *Adv. Water Resour.* **106**, 80–94.

KANG, P.K., HYMAN, J.D., HAN, W.S. & DENTZ, M. 2020 Anomalous transport in three-dimensional discrete fracture networks: interplay between aperture heterogeneity and injection modes. *Water Resour. Res.* **56** (11), e2020WR027378.

KANG, P.K., LE BORGNE, T., DENTZ, M., BOUR, O. & JUANES, R. 2015 Impact of velocity correlation and distribution on transport in fractured media: field evidence and theoretical model. *Water Resour. Res.* **51**, 940–959.

KOPONEN, A., KATAJA, M. & TIMONEN, J. 1996 Tortuous flow in porous media. *Phys. Rev.* E **54** (1), 406.

KREFT, A. & ZUBER, A. 1978 On the physical meaning of the dispersion equation and its solutions for different initial and boundary conditions. *Chem. Engng Sci.* **33** (11), 1471–1480.

KROTZ, J., SWEENEY, M.R., GABLE, C.W., HYMAN, J.D. & RESTREPO, J.M. 2022 Variable resolution Poisson-disk sampling for meshing discrete fracture networks. *J. Comput. Appl. Maths* **407**, 114094.

LICHTNER, P.C., HAMMOND, G.E., LU, C., KARRA, S., BISHT, G., ANDRE, B., MILLS, R.T. & KUMAR, J. 2015 PFLOTRAN user manual: a massively parallel reactive flow and transport model for describing surface and subsurface processes. *Tech. Rep.* LA-UR-15-20403. Los Alamos National Laboratory.

MAŁOSZEWSKI, P. & ZUBER, A. 1985 On the theory of tracer experiments in fissured rocks with a porous matrix. *J. Hydrol.* **79** (3–4), 333–358.

MAQUEDA, A., RENARD, P. & FILIPPONI, M. 2023 Karst conduit size distribution evolution using speleogenesis modeling. *Environ. Earth Sci.* **82**, 360.

MASSOUDIEH, A.M., DENTZ, M. & ALIKHANI, J. 2017 A spatial Markov model for the evolution of the joint distribution of groundwater age, arrival time, and velocity in heterogeneous media. *Water Resour. Res.* **53**, 5495–5515.

MEIGS, L.C. & BEAUHEIM, R.L. 2001 Tracer tests in a fractured dolomite: 1. Experimental design and observed tracer recoveries. *Water Resour. Res.* **37** (5), 1113–1128.

MORALES, V.L., DENTZ, M., WILLMANN, M. & HOLZNER, M. 2017 Stochastic dynamics of intermittent pore-scale particle motion in three-dimensional porous media: experiments and theory. *Geophys. Res. Lett.* **44** (18), 9361–9371.

MOURZENKO, V.V., THOVERT, J.-F. & ADLER, P.M. 2011 Permeability of isotropic and anisotropic fracture networks, from the percolation threshold to very large densities. *Phys. Rev.* E **84** (3), 036307.

NELSEN, R.B. 2013 *An Introduction to Copulas*, vol. 139. Springer Science & Business Media.

NEUMAN, S.P. 2005 Trends, prospects and challenges in quantifying flow and transport through fractured rocks. *Hydrogeol. J.* **13** (1), 124–147.

NOETINGER, B., ROUBINET, D., RUSSIAN, A., LE BORGNE, T., DELAY, F., DENTZ, M., DE DREUZY, J.-R. & GOUZE, P. 2016 Random walk methods for modeling hydrodynamic transport in porous and fractured media from pore to reservoir scale. *Trans. Porous Med.* **115**, 345–385.

PAINTER, S. & CVETKOVIC, V. 2005 Upscaling discrete fracture network simulations: an alternative to continuum transport models. *Water Resour. Res* **41**, W02002.

PAINTER, S., CVETKOVIC, V. & SELROOS, J.-O. 2002 Power-law velocity distributions in fracture networks: numerical evidence and implications for tracer transport. *Geophys. Res. Lett.* **29** (14), 1676.

PUYGUIRAUD, A., GOUZE, P. & DENTZ, M. 2019 Upscaling of anomalous pore-scale dispersion. *Trans. Porous Med.* **128** (2), 837–855.

RISKEN, H. 1996 *The Fokker–Planck Equation*. Springer.

SAFFMAN, P.G. 1959 A theory of dispersion in a porous medium. *J. Fluid Mech.* **6** (3), 321–349.

SHERMAN, T., ENGDAHL, N.B., PORTA, G. & BOLSTER, D. 2021 A review of spatial Markov models for predicting pre-asymptotic and anomalous transport in porous and fractured media. *J. Contam. Hydrol.* **236**, 103734.

VANDERBORGHT, J., MALLANTS, D. & FEYEN, J. 1998 Solute transport in a heterogeneous soil for boundary and initial conditions: evaluation of first-order approximations. *Water Resour. Res.* **34** (12), 3255–3270.

VISWANATHAN, H.S., *et al.* 2022 From fluid flow to coupled processes in fractured rock: recent advances and new frontiers. *Rev. Geophys.* **60** (1), e2021RG000744.

ZIMMERMAN, R.W. & BODVARSSON, G.S. 1996 Hydraulic conductivity of rock fractures. *Trans. Porous Med.* **23** (1), 1–30.